JACS
JOURNAL OF THE AMERICAN CHEMICAL SOCIETY
pubs.acs.org/JACS
Article

Decoding Key Transient Inter-Catalyst Interactions in a Reductive Metallaphotoredox-Catalyzed Allylation Reaction

Bart Limburg,* Àlex Cristòfol, and Arjan W. Kleij*

Cite This: J. Am. Chem. Soc. 2022, 144, 10912−10920
Read Online
ACCESS | Metrics & More | Article Recommendations | Supporting Information

ABSTRACT: Metallaphotoredox chemistry has recently witnessed a surge in interest within the field of synthetic organic chemistry through the use of abundant first-row transition metals combined with suitable photocatalysts. The intricate details arising from the combination of two (or more) catalytic components during the reaction and especially the inter-catalyst interactions remain poorly understood. As a representative example of a catalytic process featuring such intricacies, we here present a meticulous study of the mechanism of a cobalt-organophotoredox catalyzed allylation of aldehydes. Importantly, the commonly proposed elementary steps in reductive metallaphotoredox chemistry are more complex than previously assumed. After initial reductive quenching, a transient charge-transfer complex forms that interacts with both the transition-metal catalyst and the catalytic base. Surprisingly, the former interaction leads to deactivation due to induced charge recombination, while the latter promotes deprotonation of the electron donor, which is the crucial step to initiate productive catalysis but is often neglected. Due to the low efficiency of this latter process, the overall catalytic reaction is photon-limited and the cobalt catalyst remains in a dual resting state, awaiting photoinduced reduction. These new insights are of general importance to the synthetic community, as metallaphotoredox chemistry has become a powerful tool used in the formation of elusive compounds through carbon−carbon bond formations. Understanding the underlying aspects that determine the efficiency of such reactions provides a conceptually stronger reactivity paradigm to empower future approaches to synthetic challenges that rely on dual metallaphotoredox catalysis.

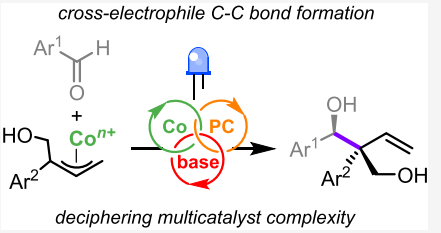

1. INTRODUCTION

Transition-metal catalysis has been paramount in the development of stereoselective carbon−carbon bond-formation reactions that are essential for the synthesis of natural products and novel pharmaceutical scaffolds. Historically, precious second- and third-row transition metals have been key catalyst components in such processes, since the reactivity and synthetic use of the more earth-abundant 3d transition metals have been much harder to control and implement. Within the era of "dual" catalytic metallaphotoredox catalysis,[1−3] the utilization of 3d transition metal-based catalysts has witnessed a remarkable revival and delivered new reactivity paradigms that are enabled through a delicate control over their available redox states, allowing productively for single-electron transfer (SET) pathways and radical-centered coupling reactions complementing the photoredox processes. In addition, the use of photoredox catalysis is beneficial as a way to avoid the preparation of organometallic precursors by generating the organometallic species *in situ* as an intermediate. This additionally amplifies the functionality in the precursors and opposes the utilization of stoichiometric reducing zerovalent metal additives (*e.g.*, Zn or Mn), which are generally less tolerant toward substrate functionality.[4,5]

The addition of a second catalytic system (or multiple systems) complicates the mechanism of the reaction,[6−10] and therefore a simplified model of the photoredox catalysis cycle is usually presented (Figure 1a), in which electrons are directly available for SET to the transition-metal catalyst following reductive quenching. However, the nature of the interactions between the photoredox catalyst and the transition-metal catalyst is likely more complex.[6,10] Furthermore, photoredox catalytic reactions are often limited by the photon flux, and thus, the usual rate-limiting steps for the transition metal-driven cycle are unlikely to apply, which has important consequences for the overall kinetics of the reaction, and therefore, for process scale-up. In order for photocatalytic processes to become generic tools in synthetic organic chemistry, it is vital to gain a deeper understanding of how the catalytic systems are intertwined and uncover the mutual influence of the separate catalytic components in relation to the overall performance of the process. A detailed knowledge of such multicatalytic approaches offers a way to create new opportunities for various transformations that operate under similar mechanistic regimes, thereby advancing this chemistry beyond empirical process optimization.

Received: April 6, 2022
Published: June 8, 2022

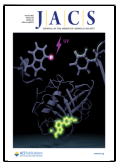

https://doi.org/10.1021/jacs.2c03692
J. Am. Chem. Soc. 2022, 144, 10912−10920

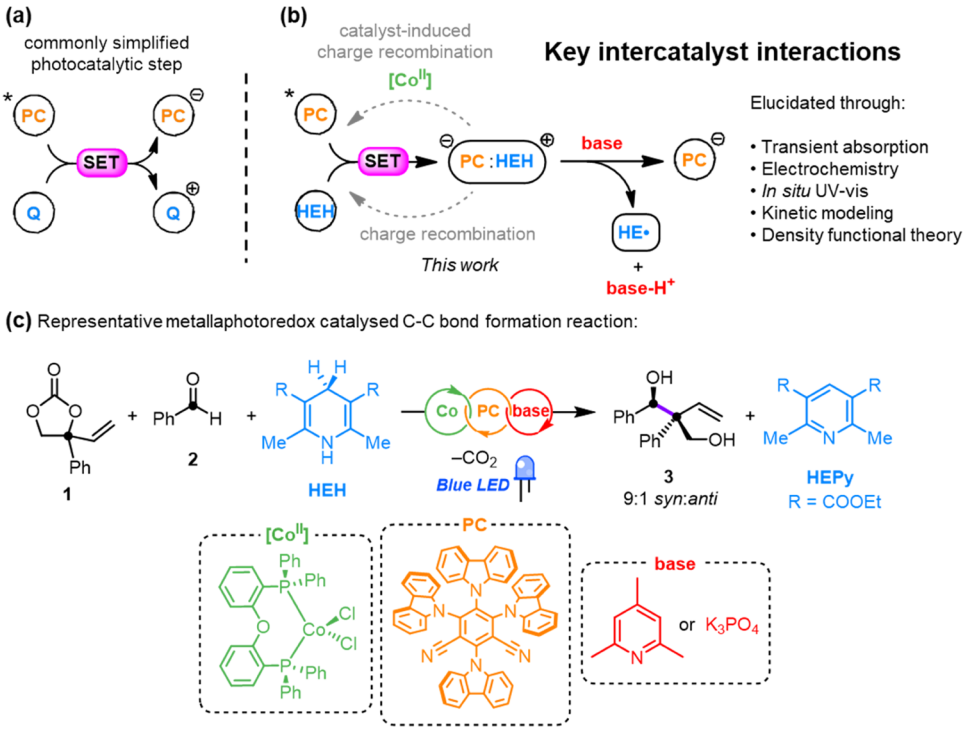

Figure 1. (a) Commonly proposed single-electron transfer (SET) step for reductive quenching, where an electron is transferred immediately from the quencher (Q) to the photocatalyst (PC), and the products ($Q^{\bullet+}$ and $PC^{\bullet-}$) are considered solubilized. (b) Important transient inter-catalyst interactions determined in this work that determine the efficiency of the representative reaction. (c) Representative metallaphotoredox catalytic cross-electrophile coupling process studied in this work.

Interest in such processes was initially focused on the combination of nickel or copper catalysis with photoredox catalysis, but recently cobalt has emerged as a potent, alternative metal in dual catalytic procedures.[11−14] While mechanistic studies for cobalt catalysis have been thoroughly probed under reductive conditions using chemical reductants[15−19] or via electrochemistry,[20] it remains uncertain whether dual metal/photoredox approaches proceed through the occurrence of similar intermediates. Several features of Co catalysis under reductive conditions remain open for debate, including the intermediacy of either Co^{I} or Co^{0}-species[5,20,21] and in dual Co/photoredox catalysis, particularly, how the effectiveness of different catalyst components and additives can be rationally optimized.

Recently, our group and several others reported stereoselective cobalt-catalyzed allylation of aldehydes as a promising new way to synthesize highly functional compounds through C−C bond formation.[21−25] Such processes are mechanistically reminiscent to other important C−C bond-formation reactions in synthetic chemistry, for which metallaphotoredox catalysis recently demonstrated to be a powerful methodology.[12,13,26−31] Here, we describe a detailed mechanistic analysis of a stereoselective C−C bond-formation reaction that can be considered as a representative example for various types of reductive dual metallaphotoredox catalytic C−C bond-formation reactions, and we give special attention to the inter-catalyst interactions (Figure 1b). Specifically, we elucidated the full mechanism of the allylation of aldehydes involving photoredox, cobalt, and base catalysis (Figure 1c). Herein, we show that the initially formed charge-separated state formed after excited-state SET is a key intermediate that requires a catalytic base to produce turnover. The same intermediate reacts counter-productively with the cobalt catalyst through an energy-wasting charge recombination path (Figure 1b). Furthermore, we demonstrate that the cobalt cycle is fast compared to the number of photons absorbed per unit time and therefore the reaction is limited by the light intensity and, as a consequence, dictated by the inter-catalyst interactions.

2. RESULTS AND DISCUSSION

2.1. Kinetics. We started our investigations by studying the kinetics of the reaction presented in Figure 1c to determine the order of reagents and the rate-limiting step. Under optimized turnover conditions as described previously,[24] using K_3PO_4 as a base, the disappearance of **1** was monitored by the evolution of its characteristic IR-band at 1815 cm^{-1} (Figure 2a). We first confirmed by NMR that the data obtained by IR corresponds to a 1:1 transformation of **1** to **3** without any observable intermediates, *i.e.*, that conversion of **1** corresponds to the formation of **3** (Figure 2a gray data). A striking observation is that the reaction rate increases until **1** has been exhausted, after which it necessarily comes to a sudden halt. This indicates, first, that the reaction is likely zero order in the substrates, and second, that a species that speeds up the reaction is formed over time. Initially, we considered that a preactivation of the catalyst was responsible for the acceleration of the reaction. However, as discussed below, the starting cobalt complex, $[Co(DPEPhos)Cl_2]$, is part of the catalytic cycle and therefore this cannot be the cause. By changing the base from K_3PO_4 to 2,4,6-collidine, we observed a higher initial rate and the reaction acceleration was less evident (Figure 2b). When the byproduct of the reaction, HEPy, is added as an additive, an intermediate rate is observed, whereas no significant differences are observed using product **3**. Therefore, the reaction follows an autocatalytic pathway, and its rate depends on the

https://doi.org/10.1021/jacs.2c03692
J. Am. Chem. Soc. 2022, 144, 10912−10920

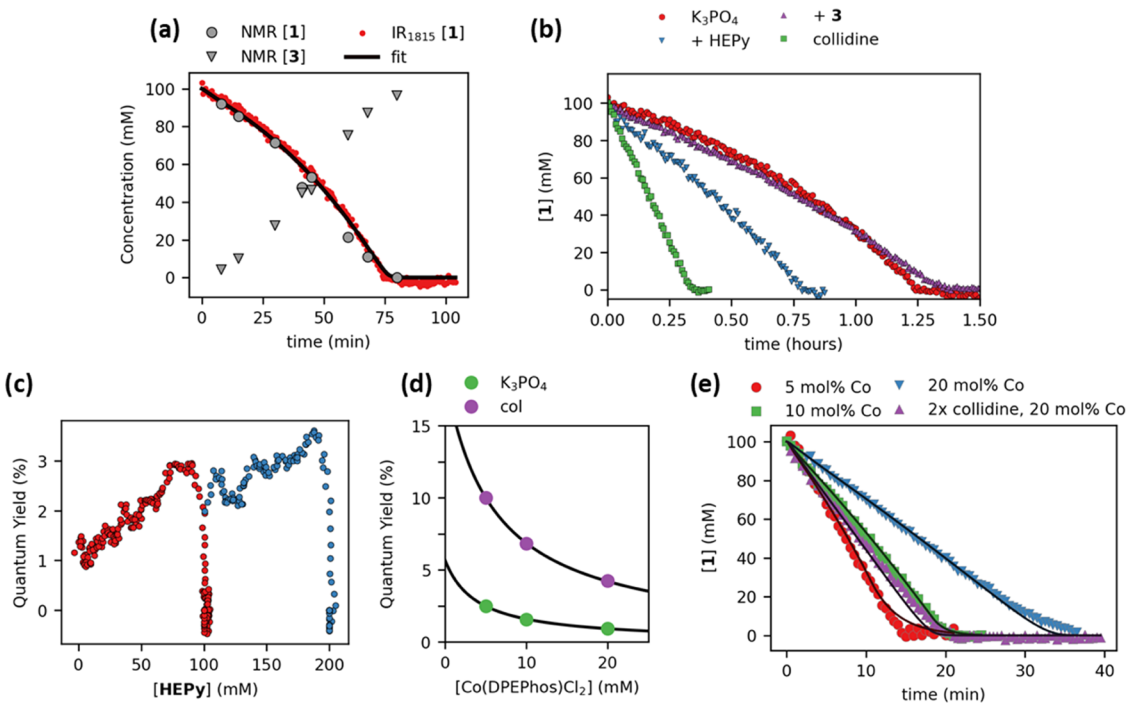

Figure 2. (a) Kinetic profile of the reaction when K_3PO_4 is used as a base. Conditions: **1** (0.1 mmol), **2** (0.15 mmol), 1,4-dihydro-2,6-dimethyl-3,5-pyridinedicarboxylic acid diethyl ester (HEH) (0.15 mmol), [Co^{II}] (10 μmol), PC (2 μmol), K_3PO_4 (0.15 mmol), THF (1 mL), and blue light-emitting diode (LED) irradiation (λ_{em} = 445 nm, 0.7 A, 1.2 μeinstein s^{-1}). Red dots: data obtained through *in situ* monitoring the C═O IR stretch frequency of **1** at 1815 cm^{-1}. Black line: fit to the kinetic model. Gray circles and gray triangles: remaining **1** and produced **3** as observed by ^{1}H NMR at different times with 1,3,5-mesitylene as internal standard. (b) Kinetic profile in the presence of different bases. The blue and purple triangles are in the presence of HEPy or **3**, respectively, in addition to K_3PO_4. The green squares are obtained by substituting K_3PO_4 with 0.15 mmol 2,4,6-collidine. (c) Quantum yield derived (using a Savitzky−Golay filter) from the kinetic trace in (b) as a function of HEPy produced during the reaction to display the autocatalytic behavior (colors match those in (b)). (d) Initial quantum yield of the reaction for the two bases as a function of the concentration of cobalt catalyst [Co^{II}], fit to the equation $y = 1/(a + bx)$, a simple model for competitive kinetics from the intermediate ^{3}[$PC^{\bullet-}$:$HEH^{\bullet+}$] (see the Supporting Information (SI)). (e) Kinetic profiles of the reaction with 2,4,6-collidine as base and different concentrations of [Co^{II}]. Solid lines: fits to the kinetic model.

basic species and their concentration. Indeed, when plotting the quantum yield of the reaction as a function of the amount of HEPy produced (assuming a 1:1 production of HEPy from the consumption of **1**), a linear increase in efficiency is observed until the reaction is exhausted (i.e., full consumption of **1**), see Figure 2c. The rate seems to follow the same linear behavior if the reaction is started with additional HEPy present, which further confirms this explanation.

We then set out to determine the influence of the light intensity and the order of substrates **1** and **2**, HEH, and [$Co(DPEPhos)Cl_2$] ([Co^{II}]). Decreasing or increasing the light intensity speeds up or slows down the reaction, indicating that the reaction is photon-limited (see the SI). The order in the substrates was further scrutinized by varying their concentrations. Neither diluting the mixture (effectively decreasing the concentration of all reagents) nor increasing the concentration of **1**, **2** or increasing the scale leads to any notable difference in the kinetic trace (see the SI). Therefore, 0th order in all reagents is confirmed, caused by the photon-limited regime. Importantly, this means that the amount of material that can be converted per unit time is limited by the light intensity. The initial quantum yield of the reaction using K_3PO_4 as the base is 1.3%, which can be increased to 7% using collidine, making the reaction more efficient and allowing more facile scale-up of the reaction mixture.

When the concentration of [Co^{II}] was varied, we did observe a change in the kinetics. Counterintuitively, increasing the concentration of [Co^{II}] leads to a slower reaction and *vice versa* (Figure 2d,e). The effect is observed both when using K_3PO_4 or collidine as the base. We initially considered that quenching of the excited state by [Co^{II}] might be responsible but quickly discarded this on the basis of Stern−Volmer analysis (see the SI), showing that [Co^{II}] does not compete with HEH for quenching of the excited state under turnover conditions. Additionally, the cobalt complex does not absorb at the irradiation wavelength, so it does not compete with light absorption. Interestingly, the lower reaction rate that results from doubling the concentration of [Co^{II}] can be counteracted by doubling the concentration of the base (see Figure 2e), suggesting that a competition between [Co^{II}] and the base exists in an intermediary step of the reaction mechanism.

2.2. Initial Photoreactions. To study the competitive effect between the base and [Co^{II}], we investigated how the reductive equivalents required for the cross-electrophile reaction are produced. Due to the use of thermally activated delayed fluorescence (TADF) photocatalyst 4CzIPN (PC), the excited-state system is complex, comprising an initial prompt fluorescent state that converts an initial singlet state to an equilibrium mixture of triplet and singlet (see the SI).[32−34] We studied the photocatalytic system using microsecond transient absorption spectroscopy (TAS). Our attention was initially focused on two specific wavelengths: 420 and 810 nm. At the former, a ground-state bleach is seen (see the SI), whereas, at the latter, a transient signal is observed (see the SI) that we

https://doi.org/10.1021/jacs.2c03692
J. Am. Chem. Soc. 2022, 144, 10912−10920

assigned to the absorbance of the ^{3}CT-state of the excited photocatalyst, as reported previously.[32] The decay-constants (τ_0 = 3.89 ± 0.05 μs) of these signals match the decay of the TADF observed by time-correlated single-photon counting (see the SI). Interestingly, upon addition of HEH, the signal at 420 nm shows the formation of a transient species that subsequently vanishes (τ = 8.2 μs, see Figure 3a; red trace

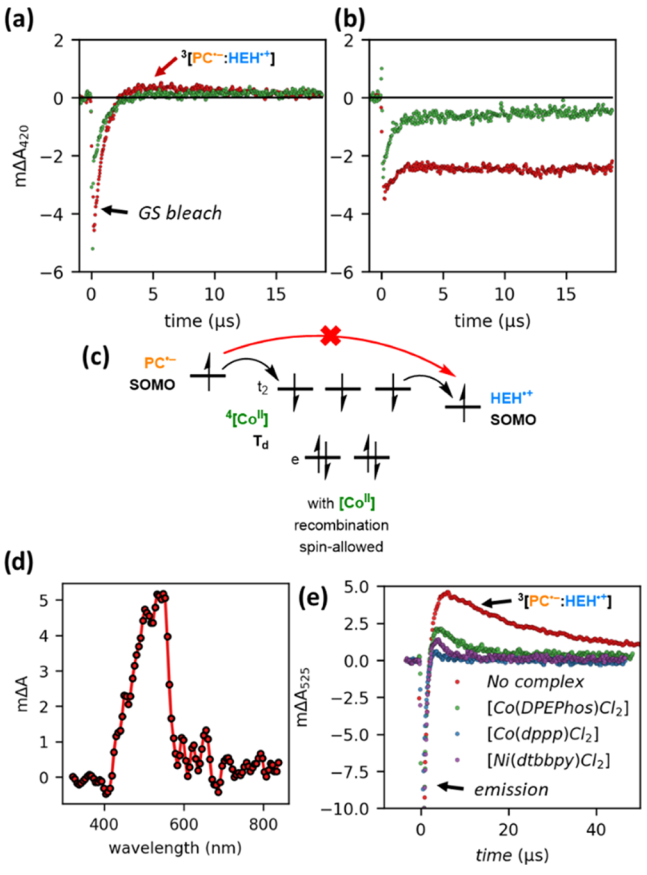

Figure 3. (a) Transient absorption spectroscopy kinetic traces at 420 nm. Conditions: PC (50 μM), HEH (200 μM) without (red) or with (green) [Co^{II}] (170 μM) in THF (3 mL). (b) Like in panel (a) but in the additional presence of 2,4,6-collidine (50 mM). (c) Simplified molecular orbital (MO) diagram showing that charge recombination from the ^{3}[PC$^{\bullet-}$:HEH$^{\bullet+}$] is spin forbidden and that in the presence of [Co^{II}], charge recombination can occur to yield an excited-state ^{2}[Co^{II}] complex that subsequently relaxes to the ground-state ^{4}[Co^{II}]. T_d = ligand field splitting in a tetrahedral environment. SOMO = Singly occupied molecular orbital. (d) Difference transient absorbance spectrum of ^{3}[PC$^{\bullet-}$:HEH$^{\bullet+}$] measured at 5 μs delay. (e) Transients at 525 nm (at the absorption maximum of ^{3}[PC$^{\bullet-}$:HEH$^{\bullet+}$]) in the absence or presence of a variety of metal complexes (170 μM).

indicated by the arrow and SI). At 810 nm, we only observed quenching of the ^{3}CT-state (τ = 0.99 ± 0.02 μs, see the SI). The transient species is assigned to a triplet charge-separated cage complex formed from the initial photoproducts: PC$^{\bullet-}$ and HEH$^{\bullet+}$. Due to the charged nature of these species, they remain in close proximity as a cage complex, ^{3}[PC$^{\bullet-}$:HEH$^{\bullet+}$], and eventually recombine to reform PC and HEH without any observable permanent charge transfer (*i.e.*, cage escape). The same experiment performed in the presence of collidine instead shows an irreversible transfer of electrons from HEH to PC, without the recovery of the ground state (Figure 3b; red trace). It is clear that the base therefore prevents charge recombination by deprotonation of the ^{3}[PC$^{\bullet-}$:HEH$^{\bullet+}$] intermediate. It is often assumed that the HEH$^{\bullet+}$-species is highly acidic and will lose a proton rapidly; here, we show that this is not generally the case, and hence the reason why photoredox catalytic reactions using HEH, or similar reductive quenchers, often require (sub)stoichiometric amounts of the base to provide productive process turnover.[12,14,35−38]

To probe the influence of the acidity of oxidized electron donor on the overall reaction, various other electron donors with more acidic protons were tried (see the SI). Only the 4-phenyl-substituted analogue PhHEH[39] yielded 60% of product **3** after 17 h of irradiation, indicating that this electron donor performs worse than HEH. Indeed, even though the proton is more acidic (calculated pK_a = −7.9 for PhHEH$^{\bullet+}$ *vs* −6.3 for HEH$^{\bullet+}$), a base is required because the solvent is not sufficiently basic (calculated pK_a = −15.5 for THF-H$^+$, see the SI). We assign the slower reaction with PhHEH to mismatches in the redox potentials (see the SI).

The competition between the base and [Co^{II}] observed during the kinetic studies led us to hypothesize that the charge-separated state ^{3}[PC$^{\bullet-}$:HEH$^{\bullet+}$] could also react with [Co^{II}]. Therefore, the traces at 420 nm of a mixture of PC and HEH were compared in the presence and absence of low concentrations of [Co^{II}]. In the presence of the cobalt complex, the charge-separated state ^{3}[PC$^{\bullet-}$:HEH$^{\bullet+}$] is no longer observed (Figure 3a, green data), indicating a fast reaction with this state. No significant change in the decay of the TA-signal at 810 nm is observed (see the SI), therefore, excluding the possibility of a (significant) reaction between the excited-state ^{3}PC with the cobalt complex prior to the formation of ^{3}[PC$^{\bullet-}$:HEH$^{\bullet+}$]. When collidine is also present in the sample, less permanent electron transfer is observed than in the absence of [Co^{II}], showing that the reaction of ^{3}[PC$^{\bullet-}$:HEH$^{\bullet+}$] with the cobalt complex is detrimental to the overall productivity of the reaction, in agreement with the observed reaction kinetics (Figure 2d,e).

We propose that the Co complex reacts with the charge-separated cage state to give quantitative charge recombination. The reason that this cage complex leads to fast charge recombination is that recombination can occur through a spin-allowed process to produce an excited-state cobalt(II) complex, removing the need for a direct spin-flip (Figure 3c). Density functional theory (DFT) calculations on [Co^{II}] indeed show that the excited (doublet) structure is only 1.1 eV (26 kcal mol^{-1}) in energy above the ground-state (quartet) structure (*cf.* the energy of the photons of 2.8 eV), which is further confirmed by the presence of absorption peaks in the NIR of the [Co^{II}]-spectrum (Figure S19). Such low-lying metal excited states may limit the quantum efficiency in metallaphotoredox chemistry involving first-row transition metals by facilitating charge recombination, reminiscent of the ultrafast deactivation of metal-to-ligand charge-transfer (MLCT) excited states in first-row transition metal complexes compared to their second- and third-row counterparts.[40−42] Indeed, we assessed the generality of the process by probing the transient absorption signal at 525 nm (the wavelength maximum of ^{3}[PC$^{\bullet-}$:HEH$^{\bullet+}$], see Figure 3d) in the presence of a variety of cobalt complexes and a nickel complex widely employed in metallaphotoredox catalysis (Figure 3e; with more example complexes in the SI). All but one of the 6 complexes reacted similarly with ^{3}[PC$^{\bullet-}$:HEH$^{\bullet+}$] with varying rates, indicating the general nature of this energy-wasting process.

https://doi.org/10.1021/jacs.2c03692
J. Am. Chem. Soc. 2022, 144, 10912−10920

2.3. Reduction of Cobalt. Having these results in hand, the reduction of [Co^{II}] was studied in detail. In recent years, several authors have suggested that the reaction follows a Co^{II}–Co^{I}–Co^{III}–Co^{II} cycle,[21−23] but compelling proof using *in situ* spectroscopy remains elusive. A cyclic voltammogram (CV) of the complex shows a reduction peak at E_p = −1.3 V *vs* Fc^+|Fc (Figure 4a; left), which can be readily reduced by $PC^{\bullet-}$ ($E_{1/2}$ = −1.63 V *vs* Fc^+|Fc). The reduction is electrochemically irreversible, but the initial [Co^{II}]-complex can be regenerated by applying more positive potentials (reoxidation peak at E_p = −0.75 V). Upon reduction to [Co^{I}], the complex likely rapidly loses a Cl^- ligand (at least up to 0.5 V s^{-1}, no direct reoxidation peak is observed) that is then replaced either by the solvent,[43,44] or the complex dimerizes to [Co(DPEPhos)-(μ-Cl)]$_2$.[18,44] Spectroelectrochemistry confirmed that the process is chemically reversible, as the initial characteristic spectrum of [Co(DPEPhos)Cl_2] can be recovered after a full CV (see the SI). After the reduction wave, the ultraviolet−visible (UV−vis) spectrum shows an altered structure in the 550−800 nm range in addition to an intense band appearing at 390 nm with clear isosbestic points at 550, 660, and 715 nm. The changed spectrum was therefore assigned to a [Co^{I}]-complex.[44] Interestingly, if the CV is measured in the presence of **1**, the reduction wave becomes completely irreversible at slow scan rates, indicating that [Co^{I}] is responsible for the oxidative addition of **1** to form a [Co^{III}-allyl] species (Figure 4a; right), confirming previous hypotheses.[22,23] At faster scan rates, the reoxidation peak reappears, allowing the determination of the rate constant of oxidative addition, k_{oa} = 1.0 M^{-1} s^{-1} (see the SI). The characteristic UV−vis spectrum of the species after oxidative addition was also obtained by spectroelectrochemistry, which looks very similar to that of [Co^{I}]. Importantly, a rate constant of this order of magnitude means that oxidative addition is not expected to limit the reaction at the initial stage when compared to a lower overall rate limited by the photon flux.

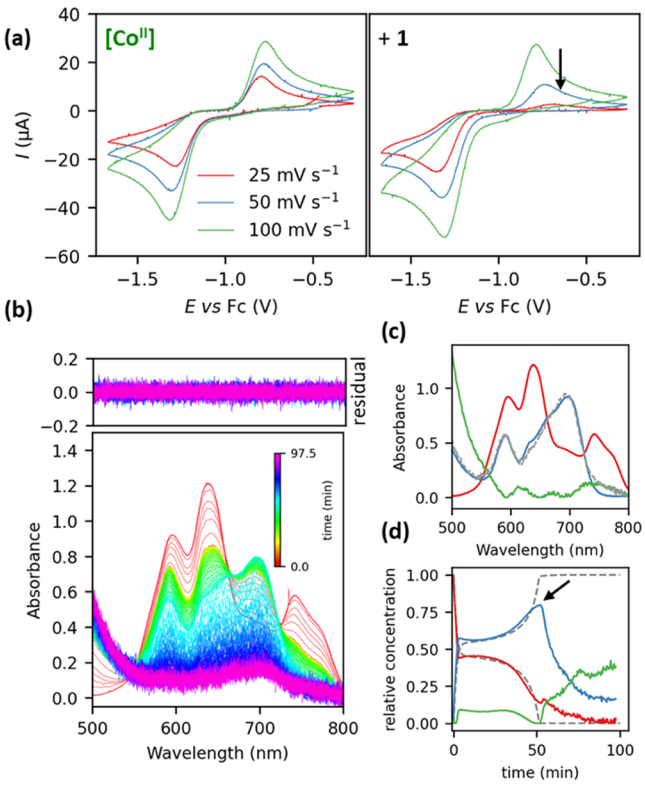

Figure 4. (a) Cyclic voltammograms of [Co^{II}] (5 mM) in the absence (left) and presence (right) of **1** (50 mM). (b) Evolution of the UV−vis spectrum under turnover conditions: **1** (0.1 mmol), **2** (0.15 mmol), HEH (0.15 mmol), [Co^{II}] (10 μmol), PC (2 μmol), collidine (0.15 mmol), THF (3 mL), blue LED irradiation (λ_{em} = 445 nm), and residual after a multivariate curve resolution fit using three spectral species. (c) Spectral species obtained from multivariate curve fit of the UV−vis data. As a reference, the spectrum obtained by spectroelectrochemistry in the presence of **1** is plotted as a dashed gray line. (d) Concentration profile of the spectral species in (c) (colors matching). The simulated cobalt species ([Co^{II}] and a mixture of [Co^{I}] and [Co^{III}-allyl]) concentrations from the kinetic model are indicated as a dashed gray line (see the SI for details). The arrow indicates the moment the spectra become noisy due to the precipitation of black metallic cobalt, coinciding with the moment the experiment and the model start to differ significantly due to exhaustion of **1**.

Using *in situ* UV−vis spectroscopy, we then monitored the spectral changes occurring under irradiation. When a mixture of [Co^{II}], PC, HEH, and collidine was irradiated, a fast conversion to a species that resembles the spectrum obtained for [Co^{I}] by spectroelectrochemistry (see the SI) was observed. After this species is formed, further reduction occurs that leads to the precipitation of a black magnetic solid that we assigned to metallic cobalt. In the absence of collidine, no significant changes in the UV−vis spectrum are observed, confirming the results obtained by TAS, showing the requirement and key role of the base in the initial processes leading to the reduction of [Co^{II}] to [Co^{I}]. Next, the spectrum was monitored under turnover conditions (in the presence of **1** and **2** and collidine, see Figure 4b). Multivariate curve resolution of the spectra shows that a photostationary state is rapidly formed, consisting of mainly two species: [Co^{II}] and an intermediate species, that matches the [Co^{III}-allyl] spectrum obtained from spectroelectrochemistry in the presence of **1** (*cf.* the blue to the dashed gray spectrum in Figure 4c), although small contributions of [Co^{I}] are likely (see the SI), as the spectra of these two species might not be distinguishable. The photostationary state evolves with the intermediate species becoming more pronounced until substrate **1** is exhausted (Figure 4d), after which precipitation of metallic cobalt occurs (indicated by the arrow in Figure 4d). A third species (green curve), which we assign to [Co^{0}], becomes significant only when the reaction is complete. These observations again indicate that the catalytic cycle is fast and therefore limited by the production of reductive equivalents through photoinduced electron transfer and thus by the light intensity. Indeed, after a further reduction of [Co^{III}-allyl] to [Co^{II}-allyl], the formation of the product and the regeneration of [Co^{II}] are fast (*vide infra*), and as such, the cobalt catalyst resting state is a mixture of mainly two species, *viz.* [Co^{III}-allyl] and the starting complex [Co^{II}], which both await further photoinduced reduction. As substrate **1** is nearing exhaustion, the rate of oxidative addition decreases, leading to an increase in the concentration of [Co^{I}]. Satisfyingly, the fitted kinetic model (*vide infra* and SI), shown by the dashed gray curves in Figure 4d captures the evolution of cobalt species during the reaction remarkably well when the intermediate species is assumed to be the sum of [Co^{III}-allyl] and [Co^{I}], whose spectra are hard to distinguish (see the SI).

2.4. Diastereoselectivity. Density functional theory (B3LYP-D3 in THF solvent, see the SI for full details) was employed to elucidate the final steps of the mechanism starting

https://doi.org/10.1021/jacs.2c03692
J. Am. Chem. Soc. 2022, 144, 10912−10920

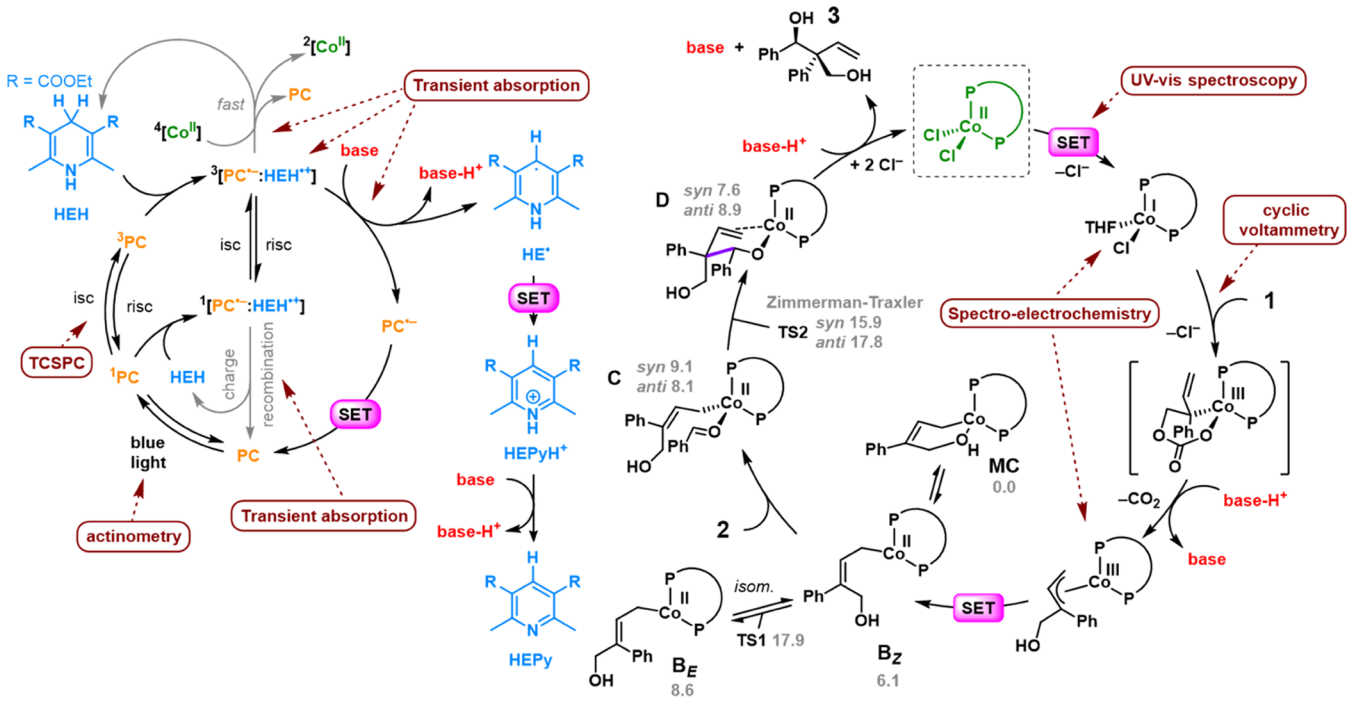

Figure 5. Full elucidated mechanism of the photoredox cycle (top) and cobalt cycle (bottom) with DFT energies (kcal mol^{-1}) in gray for selected steps. Techniques used to probe various steps in the mechanism are indicated. Only the pathway from the *Z* isomer toward the major product (*syn*) is shown; a corresponding higher energy pathway exists for the *E*-allyl isomer.

from [Co^{II}-allyl] **B** and explain the formation of the 1,3-diol **3** in a high 95:5 *syn*/*anti* ratio. Three different key steps beyond the [Co^{II}-allyl] intermediate **B** were considered: isomerization of the allylic moiety (i.e., $\mathbf{B}_Z$ to $\mathbf{B}_E$ and *vice versa*, going through tertiary-allyl species **A**, see the SI), C−C bond formation, and a protodemetalation stage. For the C−C bond formation, we optimized the pathway through well-known Zimmerman−Traxler-type transition states (TSs). In principle, four different stereoisomeric pathways can exist upon coordination of substrate **2**. The allyl species could have either an *E* or *Z* configuration, and substrate **2** could be positioned pseudo-equatorial of pseudo-axial. However, due to the steric nature of the DPEPhos ligand, we excluded the possibility of a pseudo-axial positioning of substrate **2** due to unfavorable steric 1,3-diaxial interactions.[45] Therefore, only the pathways with pseudo-equatorial aldehyde coordination and using either *E* or *Z* isomers of the [Co^{II}-allyl] **B** were considered. In addition, we considered a pathway where the pendent alcohol function was left deprotonated, but such structures lead to unfeasibly high energies for intermediates **B** and **C** and were therefore excluded (see the SI). The overall barriers for C−C bond formation are low (15.9 and 17.8 kcal mol^{-1} for forming the *syn* and *anti*-product, respectively), in agreement with a fast reaction that was observed experimentally. The protodemetalation step for the *anti*-isomer (see the SI) presents a slightly higher barrier than for the preceding C−C bond formation step, but this seems to be a minor computational artifact, as only minimal changes in the diastereoisomer ratio (*dr*) were observed experimentally when comparing different bases (see the SI for discussion).[24]

On the basis of the energies of the path (Figure 5 and SI), we therefore conclude that the stereochemistry is determined by differences in the steric requirements of the *E* and *Z*-allylic isomeric forms of the Zimmerman−Traxler TS. Isomerization of the allyl is comparable in energy to C−C bond formation, allowing interconversion of the *E* to the *Z* allyl species to give a higher amount of the *syn* product through a Curtin−Hammett scenario, in line with other reports.[46] The diastereoselectivity predicted from microkinetic modeling (96:4 *dr*, see the SI) aligns well with the experimental value (95:5 *dr*), supporting the view that the Zimmerman−Traxler TS determines the stereoselective outcome of the transformation. It should be noted that the energies of the three steps are close enough that small alterations to the system might lead to a different stereodetermining step, and therefore a large difference in *dr*. Indeed, the ligand, substrate, and the base have all been shown to influence the *dr* in varying degrees.[24] Overall, this means that although the diastereoselectivity is controlled by the cobalt cycle, the overall rate of the reaction is not.

2.5. Kinetic Modeling. Combining all observations and measured rate constants, an overall mechanism and kinetic model are proposed (Figure 5 with detailed information in the SI). In addition to the known photophysical/photochemical reactions, an additional charge-separated state (^{1}[PC$^{\bullet-}$:HEH$^{\bullet+}$]) is introduced that is formed by reductive quenching of the singlet state, which is a prevalent pathway under turnover conditions (88% of the excitations are quenched in the initial singlet state by HEH, see the SI). This species can undergo fast intersystem crossing (ISC) to form ^{3}[PC$^{\bullet-}$:HEH$^{\bullet+}$] or decay through charge recombination. Because the interconversion of ^{1}[PC$^{\bullet-}$:HEH$^{\bullet+}$] and ^{3}[PC$^{\bullet-}$:HEH$^{\bullet+}$] was not observed by TAS, these reactions are expected to be much faster than the subsequent reactions from the ^{3}[PC$^{\bullet-}$:HEH$^{\bullet+}$]-complex, and therefore the ratio of ^{3}[PC$^{\bullet-}$:HEH$^{\bullet+}$] and ^{1}[PC$^{\bullet-}$:HEH$^{\bullet+}$] are in pre-equilibrium. We therefore used the yield of intersystem crossing from the singlet state (*i.e.*, the part of ^{1}[PC$^{\bullet-}$:HEH$^{\bullet+}$] reacting through ISC *vs* charge recombination) as a fitting constant. Other unknown parameters were the rates of deprotonation by the

https://doi.org/10.1021/jacs.2c03692
J. Am. Chem. Soc. 2022, 144, 10912−10920

three bases (*i.e.*, K_3PO_4, HEPy, or collidine), as well as the rate of deactivation of $^3[PC^{\bullet-}:HEH^{\bullet+}]$ with $[Co(DPEPhos)Cl_2]$. All other unknown rate constants did not alter the overall process as long as they were sufficiently high, which can be reasonably assumed (see the SI). A global fit was performed on the *in situ* IR kinetic data, where all rate constants were shared as parameters. The excellent fit to the experimental data (see Figures 2a,e, 4d and SI) shows that the model can be validated as it well captures the important parts of the reaction path, predicts the intrinsic bottlenecks, and correctly simulates the [Co]-intermediates in the UV−vis data that was not part of the fitting dataset. Importantly, the interactions in the initial charge-separated state with either base or transition-metal catalyst are key for the efficiency of the reaction. Indeed, many of the absorbed photons are "wasted" due to recombination processes from the $^3[PC^{\bullet-}:HEH^{\bullet+}]$-intermediate. Such interactions are likely to be prevalent in many other metallaphotoredox catalysis processes, as similar reactivity was observed using various metal complexes with TAS and consequently would lead to unproductive pathways, especially when low-lying excited states are available on the transition-metal catalyst.

3. CONCLUSIONS

In summary, key inter-catalyst reactions determine the efficiency of this representative metallaphotoredox-catalyzed C−C bond-formation reaction. The base deprotonates the photochemically generated transient charge-separated cage complex, preventing rapid charge recombination that occurs in the absence of the base and thus enabling further electron transfer. The byproduct of the reaction, HEPy, is itself a base, and therefore the reaction follows an autocatalytic kinetic profile. We further show that the cobalt complex reacts competitively with the transient charge-separated state, leading to catalyst-induced charge recombination and therefore an unintuitive negative order in $[Co^{II}]$. Such counterproductive interactions are expected to be generally present in reductive metallaphotoredox catalytic reactions employing 3d metals as charge recombination in cage complexes might be facilitated by low-lying excited states of the transition-metal complex. These intricacies occurring within the SET step can easily inhibit reactions and therefore should be considered when metallaphotoredox-promoted reactions are investigated. Elucidation of the underlying mechanistic complexity of multicatalyst systems will help to further advance the field of metallaphotoredox chemistry as a powerful tool to uncover new transformations in synthetic chemistry.

■ ASSOCIATED CONTENT

Supporting Information

The Supporting Information is available free of charge at https://pubs.acs.org/doi/10.1021/jacs.2c03692.

Detailed experimental procedures, methods, and additional data related to time-correlated single photon counting; transient absorption spectroscopy; (spectro)-electrochemistry; UV−vis spectroscopy, kinetics, and density functional theory (PDF)

■ AUTHOR INFORMATION

Corresponding Authors

Bart Limburg − *Institute of Chemical Research of Catalonia (ICIQ), The Barcelona Institute of Science and Technology (BIST), 43007 Tarragona, Spain;* orcid.org/0000-0002-7996-2485; Email: blimburg@iciq.es

Arjan W. Kleij − *Institute of Chemical Research of Catalonia (ICIQ), The Barcelona Institute of Science and Technology (BIST), 43007 Tarragona, Spain; Catalan Institute of Research and Advanced Studies (ICREA), 08010 Barcelona, Spain;* orcid.org/0000-0002-7402-4764; Email: akleij@iciq.es

Author

Àlex Cristòfol − *Institute of Chemical Research of Catalonia (ICIQ), The Barcelona Institute of Science and Technology (BIST), 43007 Tarragona, Spain;* orcid.org/0000-0001-6931-6423

Complete contact information is available at: https://pubs.acs.org/10.1021/jacs.2c03692

Author Contributions

All authors have given approval to the final version of the manuscript.

Notes

The authors declare no competing financial interest.

■ ACKNOWLEDGMENTS

Professor Feliu Maseras is thanked for theoretical chemistry advice and fruitful scientific discussion. Raúl Pérez Soto is thanked for help with setting up DFT calculations. Dr. Javier Pérez is thanked for help with transient absorption spectroscopy. Dr. Marcos Gil Sepulcre and Prof. Antoni Llobet are thanked for help with spectroelectrochemistry. This project has received funding from the European Union's Horizon 2020 Research and Innovation Programme under Grant Agreement No. 889754 and from MICINN (PID2020-112684GB-100 and Severo Ochoa Excellence Accreditation 2020-2023 CEX2019-000925-S). The authors also acknowledge the Cerca program/Generalitat de Catalunya and ICREA for support.

■ REFERENCES

(1) Twilton, J.; Le, C. C.; Zhang, P.; Shaw, M. H.; Evans, R. W.; MacMillan, D. W. C. The Merger of Transition Metal and Photocatalysis. *Nat. Rev. Chem.* **2017**, *1*, No. 0052.

(2) Gualandi, A.; Anselmi, M.; Calogero, F.; Potenti, S.; Bassan, E.; Ceroni, P.; Cozzi, P. G. Metallaphotoredox Catalysis with Organic Dyes. *Org. Biomol. Chem.* **2021**, *19*, 3527−3550.

(3) Chan, A. Y.; Perry, I. B.; Bissonnette, N. B.; Buksh, B. F.; Edwards, G. A.; Frye, L. I.; Garry, O. L.; Lavagnino, M. N.; Li, B. X.; Liang, Y.; Mao, E.; Millet, A.; Oakley, J. V.; Reed, N. L.; Sakai, H. A.; Seath, C. P.; MacMillan, D. W. C. Metallaphotoredox: The Merger of Photoredox and Transition Metal Catalysis. *Chem. Rev.* **2022**, *122*, 1485−1542.

(4) Everson, D. A.; Weix, D. J. Cross-Electrophile Coupling: Principles of Reactivity and Selectivity. *J. Org. Chem.* **2014**, *79*, 4793−4798.

(5) Ma, W.-Y.; Han, G.-Y.; Kang, S.; Pang, X.; Liu, X.-Y.; Shu, X.-Z. Cobalt-Catalyzed Enantiospecific Dynamic Kinetic Cross-Electrophile Vinylation of Allylic Alcohols with Vinyl Triflates. *J. Am. Chem. Soc.* **2021**, *143*, 15930−15935.

(6) Till, N. A.; Tian, L.; Dong, Z.; Scholes, G. D.; MacMillan, D. W. C. Mechanistic Analysis of Metallaphotoredox C−N Coupling: Photocatalysis Initiates and Perpetuates Ni(I)/Ni(III) Coupling Activity. *J. Am. Chem. Soc.* **2020**, *142*, 15830−15841.

(7) Qin, Y.; Zhu, Q.; Sun, R.; Ganley, J. M.; Knowles, R. R.; Nocera, D. G. Mechanistic Investigation and Optimization of Photoredox Anti-Markovnikov Hydroamination. *J. Am. Chem. Soc.* **2021**, *143*, 10232−10242.

(8) Sun, R.; Qin, Y.; Ruccolo, S.; Schnedermann, C.; Costentin, C.; Nocera, D. G. Elucidation of a Redox-Mediated Reaction Cycle for Nickel-Catalyzed Cross Coupling. *J. Am. Chem. Soc.* **2019**, *141*, 89−93.
(9) Tian, L.; Till, N. A.; Kudisch, B.; MacMillan, D. W. C.; Scholes, G. D. Transient Absorption Spectroscopy Offers Mechanistic Insights for an Iridium/Nickel-Catalyzed C−O Coupling. *J. Am. Chem. Soc.* **2020**, *142*, 4555−4559.
(10) Qin, Y.; Sun, R.; Gianoulis, N. P.; Nocera, D. G. Photoredox Nickel-Catalyzed C−S Cross-Coupling: Mechanism, Kinetics, and Generalization. *J. Am. Chem. Soc.* **2021**, *143*, 2005−2015.
(11) Kojima, M.; Matsunaga, S. The Merger of Photoredox and Cobalt Catalysis. *Trends Chem.* **2020**, *2*, 410−426.
(12) Li, Y.-L.; Zhang, S.-Q.; Chen, J.; Xia, J.-B. Highly Regio- and Enantioselective Reductive Coupling of Alkynes and Aldehydes via Photoredox Cobalt Dual Catalysis. *J. Am. Chem. Soc.* **2021**, *143*, 7306−7313.
(13) Yasui, T.; Yamada, K.; Tatsumi, R.; Yamamoto, Y. Cobalt/Organophotoredox Dual-Catalysis-Enabled Cascade Cyclization of 1,6-Diynyl Esters via Formal 1,8-Acyloxy Migration. *ACS Catal.* **2021**, *11*, 11716−11722.
(14) Sekino, T.; Sato, S.; Yoshino, T.; Kojima, M.; Matsunaga, S. Regioselective Deaminative Allylation of Aliphatic Amines via Dual Cobalt and Organophotoredox Catalysis. *Org. Lett.* **2022**, *24*, 2120−2124.
(15) Ma, Y.; Han, Z. Computation Revealed Mechanistic Complexity of Low-Valent Cobalt-Catalyzed Markovnikov Hydrosilylation. *J. Org. Chem.* **2018**, *83*, 14646−14657.
(16) Oliveira, J. C. A.; Dhawa, U.; Ackermann, L. Insights into the Mechanism of Low-Valent Cobalt-Catalyzed C-H Activation. *ACS Catal.* **2021**, *11*, 1505−1515.
(17) Dorval, C.; Tricoire, M.; Begouin, J.-M.; Gandon, V.; Gosmini, C. Cobalt-Catalyzed C(Sp2)−CN Bond Activation: Cross-Electrophile Coupling for Biaryl Formation and Mechanistic Insight. *ACS Catal.* **2020**, *10*, 12819−12827.
(18) Friedfeld, M. R.; Zhong, H.; Ruck, R. T.; Shevlin, M.; Chirik, P. J. Cobalt-Catalyzed Asymmetric Hydrogenation of Enamides Enabled by Single-Electron Reduction. *Science* **2018**, *360*, 888−893.
(19) Gray, M.; Hines, M. T.; Parsutkar, M. M.; Wahlstrom, A. J.; Brunelli, N. A.; Rajanbabu, T. V. Mechanism of Cobalt-Catalyzed Heterodimerization of Acrylates and 1,3-Dienes. A Potential Role of Cationic Cobalt(I) Intermediates. *ACS Catal.* **2020**, *10*, 4337−4348.
(20) Hickey, D. P.; Sandford, C.; Rhodes, Z.; Gensch, T.; Fries, L. R.; Sigman, M. S.; Minteer, S. D. Investigating the Role of Ligand Electronics on Stabilizing Electrocatalytically Relevant Low-Valent Co(I) Intermediates. *J. Am. Chem. Soc.* **2019**, *141*, 1382−1392.
(21) Wang, L.; Wang, L.-J.; Li, M.; Chong, Q.; Meng, F. Cobalt-Catalyzed Diastereo- and Enantioselective Reductive Allyl Additions to Aldehydes with Allylic Alcohol Derivatives via Allyl Radical Intermediates. *J. Am. Chem. Soc.* **2021**, *143*, 12755−12765.
(22) Gualandi, A.; Rodeghiero, G.; Perciaccante, R.; Jansen, T. P.; Moreno-Cabrerizo, C.; Foucher, C.; Marchini, M.; Ceroni, P.; Cozzi, P. G. Catalytic Photoredox Allylation of Aldehydes Promoted by a Cobalt Complex. *Adv. Synth. Catal.* **2021**, *363*, 1105−1111.
(23) Shi, C.; Li, F.; Chen, Y.; Lin, S.; Hao, E.; Guo, Z.; Wosqa, U. T.; Zhang, D.; Shi, L. Photocatalytic Umpolung Synthesis of Nucleophilic π-Allylcobalt Complexes for Allylation of Aldehydes. *ACS Catal.* **2021**, *11*, 2992−2998.
(24) Cristòfol, À.; Limburg, B.; Kleij, A. W. Expedient Dual Co/Organophotoredox Catalyzed Stereoselective Synthesis of All-Carbon Quaternary Centers. *Angew. Chem., Int. Ed.* **2021**, *60*, 15266−15270.
(25) Xue, S.; Cristòfol, À.; Limburg, B.; Zeng, Q.; Kleij, A. W. Dual Cobalt/Organophotoredox Catalysis for Diastereo- and Regioselective 1,2-Difunctionalization of 1,3-Diene Surrogates Creating Quaternary Carbon Centers. *ACS Catal.* **2022**, *12*, 3651−3659.
(26) Schwarz, J. L.; Schäfers, F.; Tlahuext-Aca, A.; Lückemeier, L.; Glorius, F. Diastereoselective Allylation of Aldehydes by Dual Photoredox and Chromium Catalysis. *J. Am. Chem. Soc.* **2018**, *140*, 12705−12709.
(27) Gualandi, A.; Calogero, F.; Mazzarini, M.; Guazzi, S.; Fermi, A.; Bergamini, G.; Cozzi, P. G. Cp_2TiCl_2-Catalyzed Photoredox Allylation of Aldehydes with Visible Light. *ACS Catal.* **2020**, *10*, 3857−3863.
(28) Mitsunuma, H.; Tanabe, S.; Fuse, H.; Ohkubo, K.; Kanai, M. Catalytic Asymmetric Allylation of Aldehydes with Alkenes through Allylic C(Sp3)-H Functionalization Mediated by Organophotoredox and Chiral Chromium Hybrid Catalysis. *Chem. Sci.* **2019**, *10*, 3459−3465.
(29) Tanabe, S.; Mitsunuma, H.; Kanai, M. Catalytic Allylation of Aldehydes Using Unactivated Alkenes. *J. Am. Chem. Soc.* **2020**, *142*, 12374−12381.
(30) Gualandi, A.; Rodeghiero, G.; Faraone, A.; Patuzzo, F.; Marchini, M.; Calogero, F.; Perciaccante, R.; Jansen, T. P.; Ceroni, P.; Cozzi, P. G. Allylation of Aldehydes by Dual Photoredox and Nickel Catalysis. *Chem. Commun.* **2019**, *55*, 6838−6841.
(31) Cozzi, P. G.; Calogero, F.; Potenti, S.; Bassan, E.; Fermi, A.; Gualandi, A.; Monaldi, J.; Dereli, B.; Maity, B.; Cavallo, L.; Ceroni, P. Nickel Mediated Enantioselective Photoredox Allylation of Aldehydes with Visible Light. *Angew. Chem., Int. Ed.* **2022**, *61*, No. e202114981.
(32) Noda, H.; Chen, X. K.; Nakanotani, H.; Hosokai, T.; Miyajima, M.; Notsuka, N.; Kashima, Y.; Brédas, J. L.; Adachi, C. Critical Role of Intermediate Electronic States for Spin-Flip Processes in Charge-Transfer-Type Organic Molecules with Multiple Donors and Acceptors. *Nat. Mater.* **2019**, *18*, 1084−1090.
(33) Kobayashi, T.; Kawate, D.; Niwa, A.; Nagase, T.; Goushi, K.; Adachi, C.; Naito, H. Intersystem Crossing Rate in Thermally Activated Delayed Fluorescence Emitters. *Phys. Status Solidi A* **2020**, *217*, No. 1900616.
(34) Ishimatsu, R.; Matsunami, S.; Shizu, K.; Adachi, C.; Nakano, K.; Imato, T. Solvent Effect on Thermally Activated Delayed Fluorescence by 1,2,3,5-Tetrakis(Carbazol-9-Yl)-4,6-Dicyanobenzene. *J. Phys. Chem. A* **2013**, *117*, 5607−5612.
(35) Meng, Q. Y.; Schirmer, T. E.; Katou, K.; König, B. Controllable Isomerization of Alkenes by Dual Visible-Light-Cobalt Catalysis. *Angew. Chem., Int. Ed.* **2019**, *58*, 5723−5728.
(36) Meng, Q. Y.; Wang, S.; Huff, G. S.; Konig, B. Ligand-Controlled Regioselective Hydrocarboxylation of Styrenes with CO_2 by Combining Visible Light and Nickel Catalysis. *J. Am. Chem. Soc.* **2018**, *140*, 3198−3201.
(37) Meng, Q. Y.; Wang, S.; König, B. Carboxylation of Aromatic and Aliphatic Bromides and Triflates with CO_2 by Dual Visible-Light−Nickel Catalysis. *Angew. Chem., Int. Ed.* **2017**, *56*, 13426−13430.
(38) Wang, P. Z.; Chen, J. R.; Xiao, W. J. Hantzsch Esters: An Emerging Versatile Class of Reagents in Photoredox Catalyzed Organic Synthesis. *Org. Biomol. Chem.* **2019**, *17*, 6936−6951.
(39) Leitch, J. A.; Rossolini, T.; Rogova, T.; Dixon, D. J. α-Tertiary Dialkyl Ether Synthesis via Reductive Photocatalytic α-Functionalization of Alkyl Enol Ethers. *ACS Catal.* **2020**, *10*, 11430−11437.
(40) Auböck, G.; Chergui, M. Sub-50-Fs Photoinduced Spin Crossover in $[Fe(Bpy)3]^{2+}$. *Nat. Chem.* **2015**, *7*, 629−633.
(41) Förster, C.; Heinze, K. Photophysics and Photochemistry with Earth-Abundant Metals − Fundamentals and Concepts. *Chem. Soc. Rev.* **2020**, *49*, 1057−1070.
(42) Wegeberg, C.; Wenger, O. S. Luminescent First-Row Transition Metal Complexes. *JACS Au* **2021**, *1*, 1860−1876.
(43) Lindner, E.; Schober, U.; Glaser, E.; Norz, H.; Wegner, P. Neuartige Basische Liganden Für Die Homogenkatalytische Methanolcarbonylierung, XI [1] Ether-Phosphan-Cobalt-Komplexe in Der Katalytischen Methanolhydrocarbonylierung Zu Acetaldehyd. *Z. Naturforsch., B: J. Chem. Sci.* **1987**, *42*, 1527−1536.
(44) Aresta, M.; Rossi, M.; Sacco, A. Tetrahedral Complexes of Cobalt(I). *Inorg. Chim. Acta* **1969**, *3*, 227−231.
(45) Mejuch, T.; Gilboa, N.; Gayon, E.; Wang, H.; Houk, K. N.; Marek, I. Axial Preferences in Allylation Reactions via the Zimmerman-Traxler Transition State. *Acc. Chem. Res.* **2013**, *46*, 1659−1669.
(46) Feng, J.; Garza, V. J.; Krische, M. J. Redox-Triggered C-c Coupling of Alcohols and Vinyl Epoxides: Diastereo- and

https://doi.org/10.1021/jacs.2c03692
J. Am. Chem. Soc. 2022, 144, 10912−10920

Enantioselective Formation of All-Carbon Quaternary Centers via *Tert*-(Hydroxy)-Prenylation. *J. Am. Chem. Soc.* **2014**, *136*, 8911−8914.

https://doi.org/10.1021/jacs.2c03692
J. Am. Chem. Soc. 2022, 144, 10912−10920